microplastics

MDPI

Article

The Role of the Size and Surface Chemistry of Polystyrene Micro- and Nanobeads in the Interaction with an Advanced In Vitro Tri-Culture Intestinal Barrier Model

Stefania Mariano [1,2,*], Elisabetta Carata [3] and Elisa Panzarini [3,*]

[1] CEDAD (Centre of Applied Physics, Datation and Diagnostics), Department of Mathematics and Physics "E. De Giorgi", University of Salento, 73100 Lecce, Italy
[2] Department of Mathematics and Physics "E. De Giorgi", University of Salento, 73100 Lecce, Italy
[3] Department of Biological and Environmental Sciences and Technologies, University of Salento, 73100 Lecce, Italy; elisabetta.carata@unisalento.it
* Correspondence: stefania.mariano@unisalento.it (S.M.); elisa.panzarini@unisalento.it (E.P.)

Abstract

Micro- and nanoplastics represent ubiquitous environmental contaminants with emerging concerns regarding their impact on human health. The gastrointestinal tract is the primary site of contact, where micro- and nanoplastics may interact with the intestinal epithelium, potentially disrupting barrier integrity, altering microbiota composition, and triggering inflammatory or oxidative stress responses. Moreover, variability in particle size, shape, chemical composition, and surface modifications adds complexity to assessing their health impact. Findings remain inconsistent, and the mechanisms of toxicity are not yet fully elucidated. This study developed a tri-culture in vitro intestinal barrier model incorporating Caco-2 enterocytes, HT29-MTX mucus-secreting cells, and Raji B-induced M-like cells to mimic the structural and functional features of the human gut epithelium. Polystyrene beads of different sizes (40 nm and 200 nm) and surface functionalization (carboxylated and aminated) were characterized and exposed to the model to examine their effects on barrier integrity, cellular uptake, and cytotoxicity. The results showed that size and surface chemistry play key roles in particle interaction dynamics with the intestinal barrier, affecting cellular internalization and toxicological outcomes. This validated in vitro model provides a valuable tool for investigating micro- and nanoplastic behavior upon oral exposure, contributing to more accurate health risk assessments associated with plastic pollution.

Keywords: microplastics; nanoplastics; intestinal barrier; protein corona; tri-culture model; polystyrene nanoparticles; cellular uptake; TEER; surface functionalization; Caco-2/HT29/Raji co-culture

Academic Editor: Gary Hardiman

Received: 12 January 2026
Revised: 28 January 2026
Accepted: 5 February 2026
Published: 10 February 2026

1. Introduction

Plastics have become integral to modern life, but their widespread use has also given rise to severe pollution challenges. Micro- and nanoplastics, which are defined as plastic particles with sizes less than 5 mm and 100 nanometers, respectively, have emerged as pervasive environmental contaminants with significant ecological and health implications. The global proliferation of these particles stems from a combination of primary sources, such as microbeads in cosmetics, and secondary sources, including the fragmentation of larger plastic debris [1,2]. Microplastics, often categorized by their origins, include

primary microplastics such as resin pellets and secondary microplastics derived from the breakdown of larger plastic materials through photodegradation, mechanical abrasion, and chemical reactions [3,4]. Nanoplastics, on the other hand, result from further fragmentation of microplastics or are directly produced during industrial manufacturing processes [5]. The size distinction between these two categories has significant implications for their environmental behavior, bioavailability, and potential for toxicity [6]. As their presence in terrestrial and aquatic environments continues to rise, a growing body of research is focusing on the role that particle size and surface coatings play in determining the impacts of these contaminants [7,8].

Smaller particles, such as nanoplastics, exhibit increased surface area-to-volume ratios compared to microplastics, which enhances their interaction with surrounding media [9]. This property enables nanoplastics to bind more readily with pollutants, metals, and other contaminants, acting as vectors for the transport of hazardous substances [10]. Conversely, larger microplastics may physically obstruct the feeding mechanisms of aquatic organisms, causing direct mechanical harm [11]. These size-dependent differences in effects highlight the need to study particle size as a critical factor in understanding the ecological and health impacts of plastic pollution.

Among these, polystyrene-based micro- and nanoplastics have garnered particular attention. Polystyrene is a widely used polymer in the production of consumer goods, packaging, and insulation materials, which makes it a significant contributor to environmental plastic waste [12]. The unique characteristics of polystyrene micro- and nanoplastics, such as their lightweight structure and potential to fragment into smaller sizes, amplify their environmental presence [13]. These particles are often used as models in scientific research to understand the behavior of plastics in biological and ecological systems due to their chemical stability and ease of detection [14].

Polystyrene nanoplastics, for instance, have been shown to cause cellular stress in aquatic organisms, including oxidative damage and disruption of normal metabolic processes [14]. Their small size enables them to penetrate cellular barriers more effectively than larger particles, raising concerns about their potential bioaccumulation and toxicity [15,16]. Moreover, polystyrene surfaces readily interact with organic and inorganic pollutants, enhancing their role as vectors for secondary contamination in ecosystems [17].

In addition to size, the surface characteristics of micro- and nanoplastics play a pivotal role in shaping their environmental and biological interactions. Plastic particles rarely exist in their pristine form after entering ecosystems. Instead, they acquire a variety of surface coatings, including natural organic matter, biofilms, and adsorbed pollutants such as polycyclic aromatic hydrocarbons (PAHs) and heavy metals [18]. These coatings can significantly modify the properties of plastic particles, including their hydrophobicity, buoyancy, and chemical reactivity [19].

For example, biofilms, complex assemblages of microorganisms, can form on the surfaces of plastics, altering their interaction with marine organisms [20]. Biofilm-coated plastics may be more readily ingested by aquatic species due to the biofilm's resemblance to natural food sources, thereby increasing the likelihood of trophic transfer of plastics through the food chain [21]. Similarly, the adsorption of toxic pollutants onto the surfaces of plastics can enhance their toxicity, posing additional risks to organisms that come into contact with or ingest these particles [22]. Polystyrene micro- and nanoplastics, in particular, have been shown to acquire diverse surface coatings that increase their environmental persistence and influence their interaction with aquatic life [19].

Micro- and nanoplastics have been shown to affect various environmental compartments, including soil, freshwater systems, and marine ecosystems. Their small size enables them to penetrate deeper into sediments and tissues, while their surface coatings influence

their behavior and persistence [1]. In terrestrial environments, for instance, nanoplastics can disrupt soil microbiomes, affecting nutrient cycling and plant growth. Coatings, such as humic substances, can alter the mobility of plastics in soil and groundwater systems, affecting their distribution and potential to contaminate crops [23]. In aquatic environments, the differences in size and coatings of plastics also influence their ingestion by a wide range of organisms, from zooplankton to fish and even marine mammals [24]. Smaller particles, such as nanoplastics, can cross biological barriers, entering cells and tissues where they may induce oxidative stress, inflammation, and other adverse effects [25]. Coated plastics, on the other hand, may deliver a cocktail of toxic substances that amplify their impact on organisms. Polystyrene-based particles have demonstrated these effects prominently, showing their ability to impair reproduction and growth in various marine species [26].

Human exposure to micro- and nanoplastics is another growing concern, as these particles are increasingly detected in food, water, and air. The role of coatings, such as protein coronas formed in biological fluids, and the size-dependent uptake of plastics into cells and tissues are key areas of investigation in understanding their potential health impacts [27,28]. Early research suggests that smaller particles are more likely to translocate across biological membranes and accumulate in organs, while coatings can affect their cellular interactions and toxicity profiles [29,30].

Given the diversity of plastic types, sizes, and coatings, interdisciplinary research is essential to elucidate the full spectrum of effects associated with micro- and nanoplastics. The interactions between particle size, surface coatings, and environmental conditions require a combination of analytical techniques from materials science, toxicology, ecology, and environmental chemistry [31,32]. Advanced imaging technologies and molecular approaches are being used to characterize the physical and chemical properties of micro- and nanoplastics, while laboratory and field studies aim to uncover their impacts on organisms and ecosystems [33].

Addressing the challenges posed by micro- and nanoplastics also demands a global effort to reduce plastic pollution at its source. Strategies such as improving waste management systems, promoting the use of biodegradable materials, and reducing the release of microplastics from consumer products are critical for mitigating their impacts [34]. Additionally, policymakers and researchers must collaborate to establish standardized methods for measuring and evaluating the effects of plastic particles, particularly with respect to their size and coatings, facilitate cross-comparative studies, and inform regulatory frameworks [35].

In this study, we investigated the impact of different-sized and functionalized fluorescent carboxylate-modified polystyrene beads (200 and 40 nm (-COOH beads), green and red, respectively) and amine-modified polystyrene beads (-NH_2 beads) (200 nm, red) on an in vitro gastrointestinal barrier model developed with a tri-culture of Caco-2, HT29-MTX, and Raji B cell lines to best represent the different cell types present in the human gastrointestinal barrier.

2. Materials and Methods

2.1. Chemicals

All chemicals were of analytical grade and were purchased from Sigma-Aldrich (St. Louis, MO, USA) unless otherwise indicated.

2.2. Micro- and Nanobeads (MNBs) Characterization (TEM and DLS)

First, 200 nm green fluorescent -COOH beads (505 nm excitation, 515 nm emission), 200 nm red fluorescent -NH_2 beads, and 40 nm red fluorescent -COOH beads (580 nm excitation, 605 nm emission) were purchased from Invitrogen (Carlsbad, CA, USA). They

were functionalized with two different surface functional groups, carboxylate-modified polystyrene beads (-COOH) (200 and 40 nm, green and red, respectively) and amine-modified polystyrene beads (-NH_2) (200 nm, red). Due to their fluorescence, they are easy to detect and have been recommended for use in ecotoxicological studies [36]. The stability of the MNBs, in terms of dispersion, aggregation state, and morphology during the treatment in culture medium, was examined using transmission electron microscopy (TEM) and Dynamic Light Scattering (DLS). Aliquots of micro- and nanobeads resuspended in culture medium at T0 and after 24 h of incubation, corresponding to the time of treatment, were placed on 200-mesh copper grids and analyzed using a Hitachi HT7700 transmission electron microscope (Hitachi, Tokyo, Japan) at 100 kV.

The hydrodynamic dimensions of the MNBs were measured with the Dynamic Light Scattering technique using a Zetasizer Nano ZS90 (Malvern Instruments Ltd., Malvern, UK); the MNBs were suspended in ultrapure water.

2.3. Cell Cultures

The established cell lines were purchased from Merck Life Science Srl with the following catalog references: 86010202-1VL, Caco-2 human Caucasian colon cell line; 85011429-1VL, Raji human Negroid Burkitt's lymphoma cell line; 91072201-1VL, HT29 human Caucasian colon cell line.

The Caco-2 and Raji B cells were cultured separately in RPMI medium (Cambrex, Verviers, Belgium) supplemented with 10% heat-inactivated (56 °C for 20 min) fetal bovine serum (FBS) (Cambrex, Verviers, Belgium), 2 mM L-glutamine (Cambrex, Verviers, Belgium), 100 IU/mL penicillin–streptomycin solution, 10.000 U/mL amphotericin B (antifungal solution) (Sigma-Aldrich, St. Louis, MO, USA), and 1% non-essential amino acids (Cambrex, Verviers, Belgium) in a humidified atmosphere with 5% CO_2 at 37 °C. The HT29 cells were cultured in McCoy's 5A medium (Cambrex, Verviers, Belgium) supplemented with 10% heat-inactivated FBS (Cambrex, Verviers, Belgium), 2 mM L-glutamine (Cambrex, Verviers, Belgium), 100 IU/mL penicillin–streptomycin solution, 10.000 U/mL amphotericin B (antifungal solution) (Sigma-Aldrich, St. Louis, MO, USA), and 1% non-essential amino acids (Cambrex, Verviers, Belgium) in a humidified atmosphere with 5% CO_2 at 37 °C. Caco-2 and HT29 cells were seeded in the apical compartment at a 7:3 ratio, with a total of 2×10^5 cells in RPMI medium supplemented with 10% FBS, 2 mM L-glutamine, 100 IU/mL penicillin–streptomycin, and 1% non-essential amino acids. The co-culture was cultured for 14 days in a 5% CO_2 humidified atmosphere at 37 °C, with the culture medium changed every other day. Subsequently, 5×10^4 Raji cells were added to the basolateral compartment in RPMI medium supplemented with 10% FBS to induce the differentiation of M cells. The triple-cell culture was maintained for 5 days in a 5% CO_2 humidified atmosphere at 37 °C, with the culture medium changed every other day. For the establishment of the intestinal barrier in a triple-cell culture system, Transwell systems with polycarbonate filters featuring a 0.4 μm pore diameter and a surface area of 4.12 cm^2 (Corning Incorporated, New York, NY, USA) were used (Figure 1). To optimize the development of the tri-culture intestinal barrier model, a comparative approach was employed wherein cells were cultivated not only in the tri-culture system but also in simpler models, including mono-culture (Caco-2) and co-culture systems (Caco-2/HT29 and Caco-2/Raji B). This comparison allowed for a detailed evaluation of the distinct morphological, functional, and barrier properties characteristic of each culture condition. The morphology of the cell culture was observed by using a light microscope Eclipse 80i (Nikon, Tokyo, Japan).

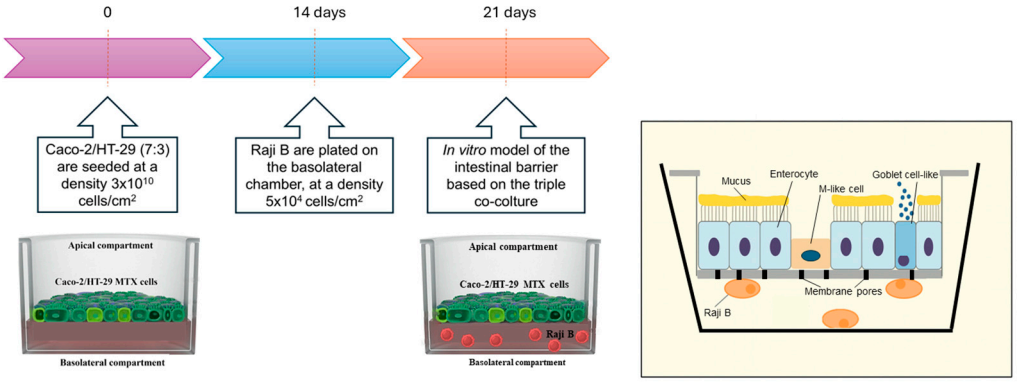

Figure 1. A schematic overview of the experimental workflow and timeline used to establish the in vitro reconstruction of the gastrointestinal barrier over 21 days using a triple-culture model (Caco-2, HT29-MTX, Raji B cells), as reported in Section 2; the schematic representation of the model is better explained on the right, reporting the presence of the components characterizing the gastrointestinal barrier in the Transwell system.

2.4. Hematoxylin/Eosin (H&E) and Alcian Blue Staining

For histological evaluation, after 21 days in culture, cells in the insert were fixed with cold methacarn solution (60% methanol, 30% chloroform, 10% acetic acid) for 1 h at 4 °C to preserve the mucus layer. After fixation, cells were rinsed thoroughly with distilled water; then, 1% Alcian blue pH 2.5 solution was subsequently added to the apical compartment and allowed to react for 30 min at room temperature to stain acidic mucins. Excess dye was removed through multiple washes with MilliQ water, and then samples were dehydrated with increasing concentrations of alcohol (70%, 95%, 100% ethanol), submerged in Xylene for 2 min and mounted with a coverslip. Layer morphology was assessed using standard hematoxylin and eosin (H&E) staining. Briefly, 4% formaldehyde-fixed cells were stained with Mayer's hematoxylin for nuclear visualization, followed by bluing under running tap water. Cytoplasmic components were counterstained using eosin Y. To ensure long-term preservation and high-resolution imaging, the stained samples were dehydrated through a graded ethanol series (70%, 95%, and 100%), cleared in xylene, and permanently mounted with a resinous medium and a coverslip. Observations were performed using a light microscope Eclipse 80i (Nikon, Tokyo, Japan).

2.5. Evaluation of Barrier's Integrity (TEER and ZO-1 Staining)

The integrity of the Caco-2-only, co-culture, and tri-culture models was evaluated by measuring transepithelial electrical resistance (TEER) using a Millicell-ERS volt/ohm meter (Merck KGaA, Darmstadt, Germany). TEER measurements were taken throughout the differentiation process every seven days during each medium replacement to monitor confluence evolution, and before and after experiments with micro- and nanobeads to evaluate barrier integrity. Only barriers with TEER values over 200 $\Omega \cdot cm^2$ were selected for permeability studies. Measurements were then performed with the tri-culture barrier model after treatments with 10 µg/mL nano- and microbeads. Treatment was stopped 24 h post exposure, followed by triple washing of the apical compartments with PBS 1X and replacement with fresh RPMI. The basolateral compartments were also emptied, washed, and refilled with fresh RPMI. The experiment was conducted in three independent replicates, each including duplicates, with measurements taken from two different points of each sample insert. TEER values were calculated using the formula $TEER = [\Omega \text{ (cell inserts)} - \Omega \text{ (cell-free inserts)}] \times 1.12\ cm^2$.

The presence of tight junctions, one of the characteristics of mature intestinal epithelium, was confirmed in the Caco-2 cell monolayer, in the Caco-2/HT29-MTX and

Caco-2/Raji B co-culture, and in the Caco-2/HT29-MTX/Raji B tri-culture by labeling the tight junction protein Zonula Occludens-1 (ZO-1). Cells were fixed with 4% paraformaldehyde in PBS for 10 min, permeabilized with 0.1% Triton™ X-100 for 10 min, and blocked with 1% BSA for 1 h at room temperature. Cells were then labeled with ZO-1 Monoclonal Antibody (ZO1-1A12) and Alexa Fluor 488 (Invitrogen, Ltd., Paisley, UK) at a concentration of 5 µg/mL in 0.1% BSA and incubated for 3 h at room temperature. After three washes with PBS (3 × 5 min), slides were covered with Mowiol 4-88 (Sigma Aldrich, St. Louis, MO, USA). Cells were analyzed using a Carl Zeiss LSM 700 laser scanning confocal microscope (Zeiss, Jena, Germany), and image acquisition was performed with ZEN software 2012 (Zeiss, Jena, Germany).

2.6. Wheat Germ Agglutinin (WGA) Conjugate Staining

To confirm the formation of M cells in the Caco-2/HT29-MTX/Raji B tri-culture model, fluorescein isothiocyanate (FITC)-labeled wheat germ agglutinin (WGA) was utilized due to its strong affinity for sialic acid and N-acetylglucosamine residues present in M-cell surfaces. Studies have demonstrated that M cells exhibit a characteristic high-intensity ring-like WGA staining pattern [37]. Tri-culture models were rinsed twice with PBS before fixation with 4% paraformaldehyde for 15 min at room temperature (RT). Following three additional PBS washes, cells were incubated with WGA-FITC conjugate (5.0 µg/mL in PBS) solution (Sigma Aldrich, St. Louis, MO, USA) for 15 min at RT. After two further PBS washes, the inserts were carefully excised and mounted onto microscope slides using Mowiol 4-88 (Sigma Aldrich, St. Louis, MO, USA). Imaging was performed a Carl Zeiss LSM 700 laser scanning confocal microscope (Zeiss, Jena, Germany), and image acquisition was performed with ZEN software (Zeiss, Jena, Germany).

2.7. Scanning and Transmission Electron Microscopy

Before exposing the barrier to micro- and nanobeads, the morphological profiles of the cells composing the barrier were analyzed using scanning electron microscopy (SEM) (Zeiss, Jena, Germany) to identify differentiated enterocytes (E), mucus-secreting cells (G), and M cells and transmission electron microscopy (TEM) to verify the ultrastructure of our model. For SEM, after being cultured as previously described, cells were first washed with cacodylate buffer (0.1 M, pH 7.4) and then fixed in 2.5% glutaraldehyde in the same buffer for 2 h on ice. Following fixation, after two washes in cacodylate buffer, post-fixation was performed in 1% OsO_4 in the same buffer for 1 h on ice. After being washed in the buffer, the cells were dehydrated using increasing concentrations of acetone: 25% (2 × 10 min at 4 °C), 50% (2 × 10 min at 4 °C), 70% (overnight at 4 °C), 90% (2 × 10 min at 4 °C), and 100% (3 × 20 min at 4 °C). Critical point drying with CO_2 was then performed using a Balzers 030 Critical Point Dryer (Balzers, Liechtenstein), followed by gold sputter coating of the samples using a Balzers SCD 050 sputter coater (Balzers, Liechtenstein). Samples were observed using a Zeiss EVO HD 15 (Zeiss, Jena, Germany) scanning electron microscope.

For TEM, cells were fixed with 2.5% glutaraldehyde in 0.1 M cacodylate buffer pH 7.4 for 1 h in ice and post-fixed with 1% OsO4 in the same buffer for 2 h in ice. Cells were stained overnight with 0.5% uranyl acetate. Cells were dehydrated with increasing degrees of ethanol (25%, 50%, 70%, 90%, and 100%) and embedded in Epoxy Spurr resin (TAAB Laboratories Equipment Ltd., Aldermaston, Berks, RG7 8NA, UK). The 60 nm sections were examined under a Hitachi 7700 (Hitachi High Technologies America Inc., Dallas, TX, USA) transmission electron microscope (TEM) operating at 80 kV.

After optimizing the in vitro intestinal barrier model, the analyses were conducted exclusively using the tri-culture.

2.8. Cell Viability (MTT Test)

After establishing the gastrointestinal barrier model as previously described, micro- and nanobeads (10 µg/mL) were added to the apical compartment in RPMI medium supplemented with 10% FBS, 2 mM L-glutamine, 100 IU/mL penicillin/streptomycin, and 1% non-essential amino acids. The cells were then incubated for 24 h in a 5% CO_2 humidified atmosphere at 37 °C. The cytotoxicity of micro- and nanobeads was assessed using the MTT assay. Cells treated with RPMI culture medium alone served as the negative control. At 24 h post treatment, the culture medium was removed, and the cells were washed twice with phosphate-buffered saline (PBS) (0.2 M pH 7.4). Fresh culture medium containing 1 mg/mL of 3-(4,5-dimethylthiazol-2-yl)-2,5-diphenyltetrazolium bromide (MTT) salt was then added to each well. Following a 2 h incubation at 37 °C in a 5% CO_2 humidified atmosphere, MTT was reduced by mitochondrial reductase in viable cells, forming formazan salt, a dark insoluble product. The formazan salts were dissolved in dimethylsulfoxide (DMSO), producing a violet solution. The absorbance of this solution was measured at 570 nm using the Ultrospec 4000 UV–visible spectrophotometer (Pharmacia Biotech, Stockholm, Sweden). Cell viability was calculated as the relative growth rate (RGR) percentage using the following formula:

$$RGR = (D_{sample}/D_{control}) \times 100 \quad (1)$$

where D_{sample} and $D_{control}$ represent the absorbances of the treated samples and the negative controls, respectively. Morphological analysis of treated and untreated cells was performed using an Eclipse 80i inverted microscope (Nikon, Tokyo, Japan).

2.9. Uptake of MNBs

After treatments on the gastrointestinal barrier model, as for the MTT test, samples were fixed with 4% paraformaldehyde in PBS (0.2 M pH 7.4) for 15 min. Subsequently, the cells were washed with 3% BSA in PBS and permeabilized with methanol for 1 min at −20 °C. Cells were then incubated for 1 h at room temperature with a blocking solution (1% BSA in PBS), followed by overnight incubation at 4 °C with a primary anti-tubulin antibody (2 µg/mL in 0.1% BSA) for samples exposed to green microbeads. After three 5 min washes, cells were incubated for 2 h with a TRITC-conjugated secondary antibody (1:50 dilution in 0.1% BSA in PBS) (Sigma Aldrich, St. Louis, MO, USA).

Cells exposed to 40 nm-sized red nanobeads and 200 nm-sized red microbeads were instead stained with FITC-conjugated phalloidin (Sigma Aldrich, St. Louis, MO, USA) to visualize actin filaments in green. Following three PBS washes, nuclei were stained with DAPI (1:1000 in distilled water) for 15 min, then washed with PBS (3 × 5 min). Slides were mounted using Mowiol® 4-88 (Sigma Aldrich, St. Louis, MO, USA). Samples were analyzed using a Carl Zeiss LSM 700 laser scanning confocal microscope (Zeiss, Jena, Germany). Image acquisition was performed using ZEN software (Zeiss, Jena, Germany).

To calculate the efficiency of internalization of MNBs, after 24 h of exposure, the total medium was collected, the wells were washed twice with PBS, and fluorescence was measured with a Synergy HT Multi-Detection Microplate Reader (Agilent, Santa Clara, CA, USA) at excitation/emission wavelengths of 505/515 nm and 580/605 nm for green and red MNBs, respectively. The obtained values were converted into MNB concentrations, based on the controls (DMEM with the same concentration of each particle type used). The reported percentages of translocation are the MNB amounts in the samples divided by the MNB amounts to which cells were exposed.

2.10. Assessment of Protein Corona

MNBs at a concentration of 10 µg/mL were incubated with the tri-culture gastrointestinal barrier model for 24 h at 37 °C, following the method described by

Lundqvist et al. (2008) [38]. To eliminate loosely bound proteins, the samples were subjected to three rounds of washing via centrifugation (18,000 rpm, 15 °C, 40 min). After each centrifugation, the pellet was resuspended in 1 mL of PBS and transferred to a fresh tube. The final pellet was resuspended in Laemmli Sample Buffer (BIO-RAD, CA, USA) containing β-mercaptoethanol (Sigma; Steinbach, Germany). The samples were then boiled for 5 min. Following this, another centrifugation step was performed to separate the particles from the proteins that had desorbed from their surfaces. The resulting protein-containing supernatant was loaded onto an SDS-PAGE gel for analysis. One-dimensional polyacrylamide gel electrophoresis (SDS-PAGE) was conducted using 12% polyacrylamide gels with a thickness of 1 mm (Mini-PROTEAN TGX Gels, BIO-RAD, CA, USA), operated at 90 V for approximately 80 min. Each gel included a molecular weight marker ranging from 10 to 180 kDa (Proteintech, Rosemont, IL, USA). Following electrophoresis, the gel was washed in water, then stained with Bio-Safe Coomassie Stain G-250 (BIO-RAD) for 1.5 h. Gel was subsequently destained through repeated washes in a solution of 40% methanol and 10% acetic acid. Gel imaging was carried out using Chemidoc (BIO-RAD, Hercules, CA, USA) and densitometric analysis was conducted with ImageJ software 1.54p.

2.11. Statistical Analysis

Experiments were performed in three independent biological replicates (n = 3), each including two Transwell inserts per condition (technical replicates, n = 2 inserts/replicate). Data are presented as the mean ± SD from a total of 6 inserts per condition, with statistical significance determined by one-way ANOVA followed by Tukey's post hoc test ($p < 0.05$).

3. Results and Discussion

3.1. Stability of MPs and NPs

The measured hydrodynamic average sizes at T_0 for the functionalized micro- and nanoplastics, 272.4 ± 62.5 nm (200 nm -COOH, sample a), 39.4 ± 15.2 nm (40 nm -COOH, sample b), and 265 ± 45.2 nm (200 nm -NH_2, sample c), suggest good monodispersity, particularly considering the inherent variability associated with particle synthesis and surface functionalization. After 24 h of incubation in DMEM, no significant changes in hydrodynamic diameter or signs of aggregation were observed. This indicates strong colloidal stability, which is crucial for particle behavior in biological systems (Figure 2).

Average hydrodinamic diameter / nm ± σ			
	200 nm (-COOH) green	40 nm (-COOH) red	200 nm (-NH_2) red
T_0	272.4 ± 62.5	39.4 ± 15.2	265 ± 45.2
24h	326.2 ± 75.1	57.2 ± 17.5	289.5 ± 24.9

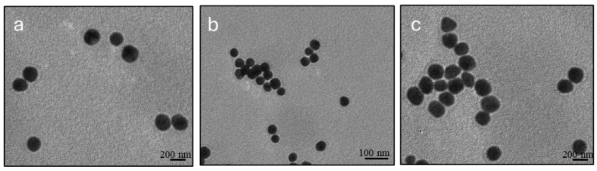

Figure 2. Average hydrodynamic diameters (DLS) of carboxylated polystyrene (PS-COOH) and aminated polystyrene (PS-NH_2) in DMEM at T0 and after 24 h in complete DMEM medium culture. TEM micrographs of 200 nm -COOH MPs (**a**), 40 nm -COOH NPs (**b**), and 200 nm -NH_2 MPs (**c**) after 24 h in complete DMEM medium culture.

3.2. Cell Model Characterization: Assessment of Cell Barrier Formation

The current study aimed to demonstrate the successful establishment of a 3D intestinal in vitro model composed of differentiated enterocytes, mucus-secreting cells, and M-like cells for studying the impact and internalization of nano- and microplastics. Optimization of the intestinal epithelial barrier model was carried out by comparing different culture configurations based on Caco-2 cells. Initially, human colorectal adenocarcinoma Caco-2 cells in mono-culture were used to establish baseline barrier properties, as these cells are widely recognized for their ability to acquire morphological and functional characteristics very

similar to enterocytes upon differentiation and the consequent formation of a monolayer with tight junctions, apical and basolateral sides, and a brush border with microvilli on the apical surface. Subsequently, co-culture systems combining Caco-2 with HT29 or Raji B cells were evaluated in order to better mimic the complexity of the intestinal epithelium, incorporating mucus-secreting and immune-related components. HT29 cells, in particular, are capable of secreting vacuoles filled with mucin, providing a protective extracellular mucus layer and mimicking goblet cell function. The in vitro system was further enhanced by adding Raji B cells (lymphoblast-like) to the Caco-2/HT29 co-culture. These cells are incorporated into the basolateral chamber of the insert on which the Caco-2/HT29 cells grow to induce the differentiation of Caco-2 cells towards a microfold (M) cell phenotype. M cells are specialized cells with the ability to transport particulate matter via endocytosis, such as bacteria, viruses, nanoparticles, and microparticles [39]. The optimization process therefore relied on a stepwise comparison among mono-culture, co-culture, and tri-culture systems to select the most physiologically relevant model. This complex system offers a physiologically relevant platform for studying intestinal barrier properties and interactions with exogenous compounds, including micro- and nanoplastics [39].

3.3. Barrier Morphology and Functionality

Phase-contrast microscopy (Figure 3a–d) revealed progressive cellular morphological maturation and functional specialization across intestinal barrier models, with mucus secretion (M) emerging as a hallmark of co-culture complexity. Monolayer Caco-2 cells (Figure 3a) exhibited a typical cobblestone morphology characteristic of differentiated enterocytes, while co-culture with HT29 cells (Figure 3b) introduced prominent mucus-producing goblet cells, visible in the figure as gray dense regions. The addition of Raji B cells (Figure 3c) maintained epithelial integrity without mucus, but the tri-culture of Caco-2/HT29/Raji B (Figure 3d) displayed optimal physiological relevance, featuring dense mucus layers that mimic the native intestinal mucus barrier. Hematoxylin–eosin staining (Figure 3e) confirmed the formation of a continuous epithelium indicative of robust cell–cell adhesion essential for barrier function. Alcian blue staining (Figure 3f) specifically highlighted acidic sulfated mucins (blue) secreted by HT29-derived goblet cells like within the tri-culture model.

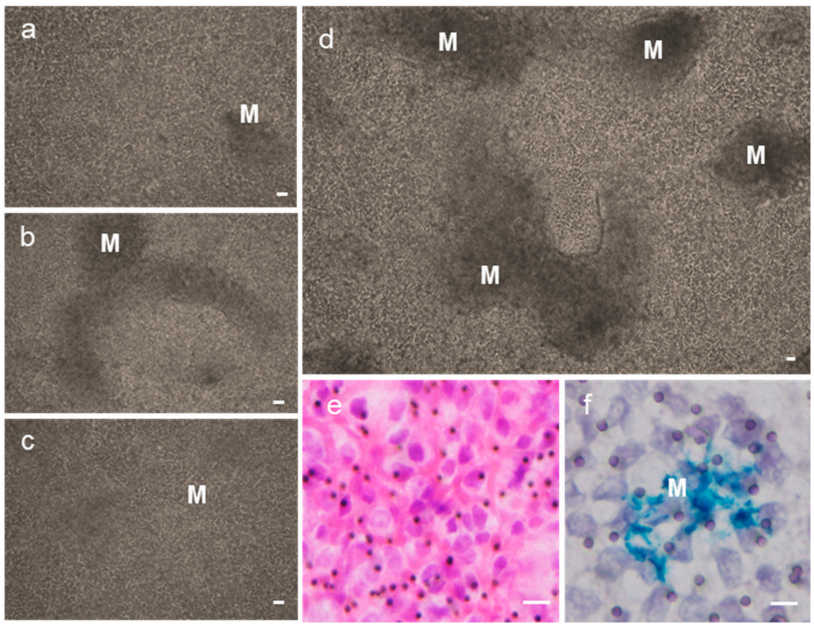

Figure 3. (**a**–**d**) Live-cell phase-contrast microscopy (inverted microscope) showing cellular morphology and mucus secretion (M) in (**a**) Caco-2 cells; (**b**) Caco-2/HT29 cells; (**c**) Caco-2/Raji B cells; and

(**d**) Caco-2/HT29/Raji B cells. M = mucus. Bar = 20 µm. (**e**) Hematoxylin–eosin (H&E) staining reveals the formation of a continuous epithelium. (**f**) Alcian blue staining highlights acidic mucins (blue) in mucus-producing cells; M = mucus. Bar = (**e**,**f**) 5 µm.

Once the morphological organization of the cell monolayers in terms of cell growth, confluence, and the formation of mucus was confirmed by optical microscopy, transepithelial electrical resistance (TEER) measurements were performed to quantitatively evaluate barrier formation and tight junction functionality (Figure 4). TEER measurements confirmed the formation of a mature and functional epithelial barrier. The observed TEER values above 200 $\Omega \cdot cm^2$ are in line with recent findings from advanced tri-culture intestinal models, which demonstrate strong barrier properties and effective tight junction assembly [40,41]. Such TEER stability reflects the development of a well-organized epithelial monolayer capable of regulating paracellular transport and maintaining selective permeability. The mono-culture of Caco-2 cells routinely generates high TEER values, often over 200 $\Omega \cdot cm^2$ depending on experimental conditions, cell passage, and measurement systems, demonstrating pronounced tight junction formation and low paracellular permeability. This is consistent with our measured value of $387 \pm 3.5\ \Omega \cdot cm^2$, which falls within published ranges for Caco-2 mono-cultures. When Caco-2 cells are co-cultured with HT29 MTX cells, which produce mucus, or with immune-like Raji B cells, the TEER values decrease noticeably ($275 \pm 5.8\ \Omega \cdot cm^2$ for HT29 MTX co-culture; $268 \pm 4.3\ \Omega \cdot cm^2$ for Raji B co-culture). This reduction is well documented in the literature, as the inclusion of goblet-like cells and immune components tends to modulate tight junction assembly and more closely approximates the leaky and dynamic nature of the intestinal epithelium in vivo. The triple co-culture model (Caco-2/HT29 MTX/Raji B) yields a TEER value of $354 \pm 6.9\ \Omega \cdot cm^2$. Intriguingly, this value is higher than that of either double co-culture (Caco-2/HT29 MTX or Caco-2/Raji B alone) but remains lower than that of the Caco-2 mono-culture. This suggests that the combined presence of mucus-producing and immune-like cells supports moderate tight junction integrity, while retaining essential physiological features. The literature reports comparable values for these complex models, underscoring their relevance for mimicking the intestinal barrier for absorption, transport, and toxicity studies. The high TEER values observed in intestinal co-culture models result from the complex interaction among absorptive enterocytes, mucus-secreting goblet cells, and immune-like cells, which together promote robust barrier integrity. Goblet cells contribute to increasing TEER values by secreting mucins that form the protective mucus layer, reducing passive permeability and enhancing barrier function, as demonstrated particularly in Caco-2 and HT29 co-cultures [42]. Immune cells, such as macrophage-like cells incorporated in advanced triculture models, further modulate barrier stability via cytokine signaling, influencing tight junction protein expression and organization [43]. Maintaining elevated TEER is essential for in vitro intestinal models to reliably simulate nutrient absorption, drug transport, and nanoparticle uptake, offering physiological fidelity to human gut functions. Robust barrier integrity indicated by high TEER is critical for toxicology and disease modeling to avoid confounding by barrier disruption, ensuring accurate interpretation of experimental outcomes [44].

The maturation and maintenance of tight junction proteins, such as claudins, occludin, and zonula occludens-1 (ZO-1), are essential for establishing high TEER and low paracellular permeability. ZO-1 staining revealed continuous and well-defined fluorescence along intercellular boundaries in all culture conditions, including Caco2, Caco2-HT29, Caco2 Raji B, and the Caco2-HT29/Raji B triple-culture system (Figure 4a–d). This finding confirms the establishment of functional tight junctions (Figure 4e,f), a critical feature ensuring epithelial barrier integrity and precise regulation of paracellular transport. The organized localization of ZO-1 indicates the presence of a mature, cohesive epithelial monolayer

capable of regulating permeability and maintaining selective barrier function, as supported by recent advanced in vitro intestinal models [45,46].

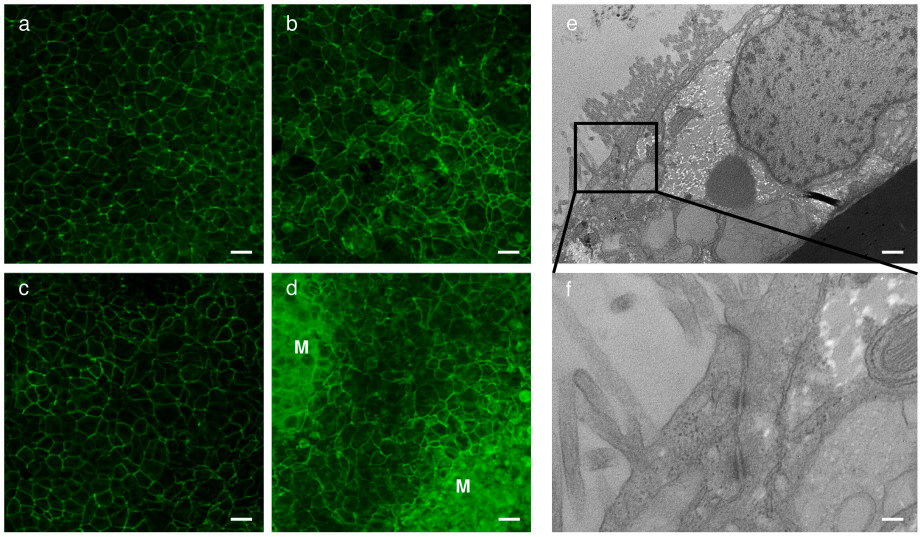

TYPE OF CELLS IN CULTURE	TEER (Ω·cm²)
Caco-2 cells	387 ± 3.5
Caco-2 cells/HT-29 MTX cells	275 ± 5.8
Caco-2 cells/Raji B cells	268 ± 4.3
Caco-2 cells/HT-29 MTX/Raji B cells	354 ± 6.9

Figure 4. Confocal microscopy micrographs of Caco-2 cells (**a**), Caco-2/HT29 co-culture (**b**), Caco-2/Raji B co-culture (**c**), and Caco-2/HT29/Raji B tri-culture (**d**), following immunolabeling of the tight junction protein ZO-1 with the ZO-1 Alexafluor 488 monoclonal antibody. In (**d**), increased fluorescence is observed corresponding to mucus (M) accumulation zones. Bar = 10 μm. (**e**,**f**) Transmission electron microscopy images of the Caco-2/HT29-MTX/Raji B tri-culture intestinal barrier model. The magnification image (**f**) highlights a tight junction indicative of robust paracellular barrier integrity. Bar = (**e**) 2 μm; (**f**) 500 nm.

Recent research highlights the enhancement in tight junction protein expression, including ZO-1, in tri-culture systems that integrate immune cell components such as Raji B cells, which better mimic the in vivo microenvironment of the intestinal mucosa. This co-culture induces signaling pathways that promote tight junction assembly and overall barrier robustness [42,47]. Additionally, the presence of mucus-producing cells in the co-culture further supports tight junction stability by creating a protective mucosal environment [45]. These observations establish the tri-culture and related co-cultures as valuable models for studying intestinal permeability, drug transport, and barrier dysfunction in response to external stimuli, including pathogens and nanomaterials. The findings agree with contemporary protocols that emphasize tight junction integrity as a critical endpoint for validating in vitro intestinal epithelium models [42,47].

3.4. Cell Morphology and Specialization

The SEM analysis performed on the 3D culture revealed the cell types characterizing the gastrointestinal barrier, i.e., enterocytes (E), goblet-like cells (G), and M cells (M) (Figure 5a–e). The observation of abundant mucus-producing cells (Figure 5a,c) significantly enhances the model's physiological relevance to the gastrointestinal barrier. Recent research, including that by Santoni et al. (2025) [48], demonstrates that the inclusion of HT29-MTX cells in tri-culture models robustly promotes mucus layer formation. This mu-

cus acts as a selective barrier, modulating epithelial permeability and providing protection against pathogenic and chemical insults, thus closely resembling the structure–function relationships found in vivo [49].

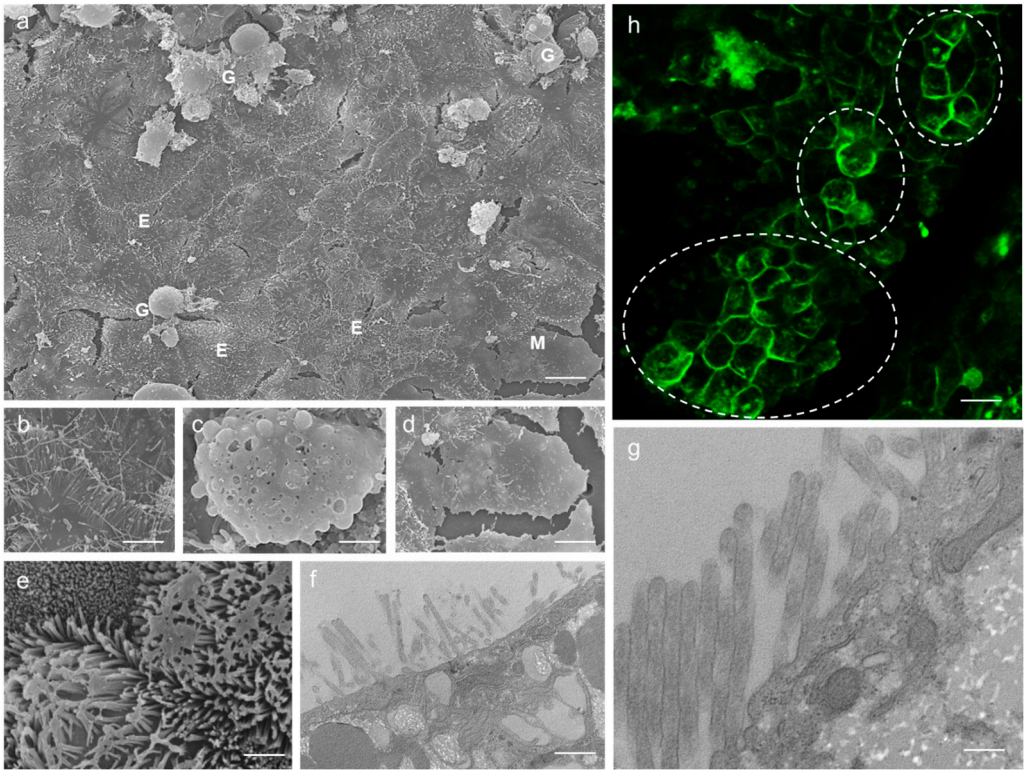

Figure 5. SEM analysis of the intestinal barrier model based on the co-culture of three cell lines (**a**) (G = Goblet cell like). M cells (M) were identified based on the absence of microvilli on the cell surface, whereas Caco-2 cells (E) display microvilli organized into the typical brush border of enterocytes (**b**,**e**). In (**c**), details of mucus-secreting HT29 cells are shown. In (**d**), details of an M cell are shown. The rupture along intercellular junctions is an artifact of the SEM sample preparation procedure. Bar = (**a**) 10 μm; (**b**–**d**) 5 μm; (**e**) 2 μm. In (**h**), a confocal microscopy image acquired after labeling with wheat germ agglutinin (WGA) lectin to evaluate the differentiation of Caco-2 cells into M cells in the presence of Raji B cells is shown. Bar = 10 μm. In (**f**) and (**g**), TEM micrographs show apical microvilli arranged to form the characteristic brush border of enterocytes. Bar = (**f**) 10 μm, (**g**) 1 μm.

The highly differentiated morphology of enterocytes, distinguished by dense and uniform apical microvilli forming a well-defined brush border, an established hallmark of absorptive function in the intestinal epithelium, is reported in Figure 5e–g. This structural organization is a recognized indicator of cell polarization and epithelial maturation, as highlighted in recent standardized approaches for advanced in vitro intestinal models [42,48]. The identification of M-like cells, recognized by the absence of apical microvilli (Figure 5d), is in line with the well-characterized process through which the presence of Raji B cells in the Caco-2/HT29 co-culture promotes M-cell differentiation in Caco-2 cells. Such morphological changes closely mirror the transformation mechanisms demonstrated in contemporary studies [48]. Moreover, wheat germ agglutinin (WGA) staining displayed strong fluorescence intensity across the cells, supporting the presence of M-like cells in our gastrointestinal barrier (Figure 5h). WGA selectively binds to terminal N-acetylglucosamine and sialic acid residues, which are highly expressed on the apical surface of M cells. This glycan enrichment provides a reliable biochemical signature for identifying M-cell populations within differentiated intestinal models [48,50]. These M-like cells represent a critical population for investigations into antigen sampling, translocation, and interaction with

gut luminal contents. By integrating enterocyte polarization, M-cell differentiation, and mucus secretion, our results confirm the tri-culture system's ability to recapitulate the complex functions and microarchitecture of the human intestinal epithelium. This model not only ensures more accurate predictions in permeability and immunity studies but also aligns with the most recent literature and regulatory standards for in vitro intestinal systems [42,48,49].

The efficient differentiation of M-like cells in the co-culture model supports its applicability in mechanistic investigations of nanoparticle translocation and antigen sampling across the intestinal barrier. Modern nanotoxicology studies highlight the importance of M cells as preferential sites for particulate uptake and transepithelial transport.

Rejinold et al. (2025) [45] contributed insights into the microenvironment and immune cross-talk, emphasizing the functional role of the glycocalyx marked by WGA in mediating epithelial–immune cell communications. Wang et al. (2025) [46] developed bioactive nanomotors capable of efficient passage through the intestinal barrier by interacting with mucosal glycocalyx structures highlighted by WGA staining, demonstrating the importance of this epithelial feature for nanoscale transport regulation. Previous work by Vincentini et al. (2022) [49] demonstrated that WGA staining reliably indicates the differentiation and mucus production in advanced in vitro intestinal barrier models, supporting functional barrier properties for nanoscale transport and immune interactions. Santoni et al. (2025) [48] further validated this by showing enhanced mucus continuity and faster epithelial differentiation in co-culture models under mechanical stimulation, with WGA marking the mucus layer integrity crucial for physiological relevance.

3.5. Internalization and Cytotoxicity of MNBs in 3D Cell Model

The internalization of plastic particles by our in vitro gastrointestinal barrier model based on the tri-culture of Caco-2, HT29-MTX, and Raji B cell lines was determined by confocal microscopy and by evaluating the presence of MNBs in the culture medium after 24 h of exposure of the barrier. A single mass-based concentration (10 µg/mL) and a 24 h exposure period were selected, in line with commonly used in vitro micro/nanoplastic protocols, with the primary aim of validating and functionally characterizing the advanced intestinal barrier model rather than performing an extensive dose– and time–response analysis. Previously, we evaluated the impact of plastic beads on the viability of cell-forming barriers and on TEER values (Figure 6C).

In general, the obtained data demonstrate that carboxylated polystyrene nanobeads show a much greater cytotoxic effect toward intestinal epithelial cells than larger microscale particles or amine-modified variants. Exposure of the 3D cultures to polystyrene micro- and nanobeads for 24 h led to a substantial decrease in barrier function and viability across all particle types, as illustrated in Figure 6A. The effect is most pronounced for the 40 nm (-COOH) red nanobeads, where the reduction is significantly greater than with either 200 nm (-COOH) green or 200 nm (-NH_2) red beads. This outcome suggests that smaller particles with carboxylate surface groups disrupt the intestinal epithelium more efficiently than larger or aminated beads. Recent research confirms that nanoparticle size and charge are pivotal in determining epithelial disruption and permeability: negatively charged surfaces such as –COOH can interact more strongly with cell membranes and tight junction proteins, impairing barrier resistance measured as TEER [51–53]. Moreover, these findings reflect the complex interplay between mucus, epithelial, and immune cell components in 3D co-culture models that more accurately mimic physiological responses compared ro mono-cultures. Studies further note that small, highly charged particles can trigger oxidative stress, inflammation, and cytoskeletal rearrangement, all of which compromise cellular integrity, as observed in the greater decrease for 40 nm (–COOH) beads [54].

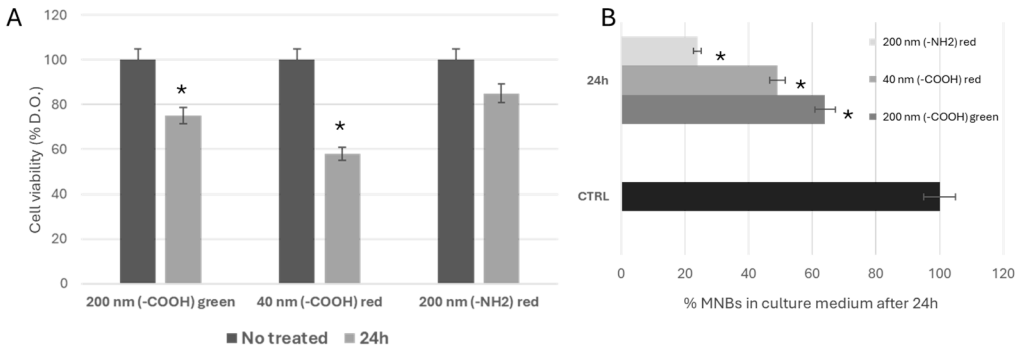

C

MICRO- OR NANOBEADS	TEER ($\Omega \cdot cm^2$) OF 3D CULTURE
200 nm (-COOH) green	210 ± 3.5
40 nm (-COOH) red	195 ± 5.8
200 nm (-NH_2) red	256 ± 4.3

Figure 6. (**A**) Cell viability (MTT assay) of the intestinal barrier model based on the co-culture of three cell lines treated with 10 µg/mL of 200 nm (PS-COOH), 40 nm (PS-COOH), and 200 nm (PS-NH_2). The viability measured as indicated in the Methods Section represents the values as a percentage of the respective control (untreated cells) values from three independent experiments. Asterisks indicate significant values ($p < 0.05$) from the respective untreated control cells. (**B**) Analysis of internalization efficiency by measuring the amount of MNBs remaining in the culture medium of the intestinal barrier 24 h after treatment with 10 µg/mL of MNBs. The values are reported as percentages relative to the control (10 µg/mL MNBs in DMEM) from three independent experiments. Asterisks indicate significant values ($p < 0.05$) from the respective untreated control cells. (**C**) TEER measurement for the evaluation of tri-culture barrier integrity at 24 h after treatment with 10 µg/mL of MNBs. The values are reported from three independent experiments.

Interestingly, 200 nm-sized aminated beads appear less damaging. Positively charged nanoparticles, such as aminated (-NH_2) polystyrene beads, often demonstrate reduced cytotoxicity in intestinal barrier models compared to negatively charged counterparts. This phenomenon is explained by their electrostatic interactions with the intestinal mucus layer, which is rich in negatively charged glycoproteins (mucins). The positive surface charge promotes stronger adhesion to the mucus, effectively trapping the nanoparticles within the mucus and limiting their direct contact with epithelial cells. This sequestration reduces cellular uptake and the resultant cytotoxic stress on epithelial cells, thereby preserving barrier integrity [53,55]. Moreover, mucus entrapment delays or prevents nanoparticle penetration to the epithelial surface, which decreases the induction of reactive oxygen species (ROS), inflammation, and apoptosis, common mechanisms by which nanoparticles induce cytotoxicity. Studies have shown that positive charge favors the retention of particles in the luminal mucus, acting as a physical barrier against epithelial disruption, whereas negatively charged particles tend to diffuse more freely through the mucus and interact with cell membranes [46,56].

The evaluation of uptake of plastic particles corroborates the observed effects on barrier integrity. Our results reveal a clear effect of both nanoparticle size and surface functionalization (-NH_2 vs. -COOH groups) on cellular internalization, as reflected by the percentage of micro/nanoplastics (MNBs) remaining in culture medium after 24 h (Figure 6B). In particular, 200 nm-sized (-NH_2) red particles show the lowest percentage left in the medium after 24 h, meaning that they have been internalized by cells to a greater extent compared to both 40 nm-sized (-COOH) red and 200 nm-sized (-COOH) green particles. This trend highlights the dual influence of size and surface chemistry.

Studies such as Marcellus et al. (2025) [57] and Zhang et al. (2025) [58] found that among polystyrene plastic particles, those with smaller dimensions and a higher surface area produced more extensive membrane damage and were taken up more efficiently by intestinal cells. They often triggered oxidative stress and inflammatory signaling pathways, which lead to cell dysfunction and death. Other works, including Kustra et al. (2025) [59] and Domenech et al. (2021) [60], observed that nanoplastics cause pervasive sublethal stress: they do not always kill cells immediately but can alter gene expression linked to DNA repair (including base excision and double-stranded break repair) and reduce the cells' ability to recover from further injury, thus increasing the risk of genome instability and long-term health effects. Carboxylation on the surface further enhances these interactions, increasing cytotoxicity compared to neutral or amine-modified surfaces.

Confocal microscopy analysis confirmed that all tested polystyrene particles were successfully internalized by our gastrointestinal barrier model, demonstrating their strong ability to penetrate cellular barriers, as shown in the confocal and z-stack mode images reported in Figure 7.

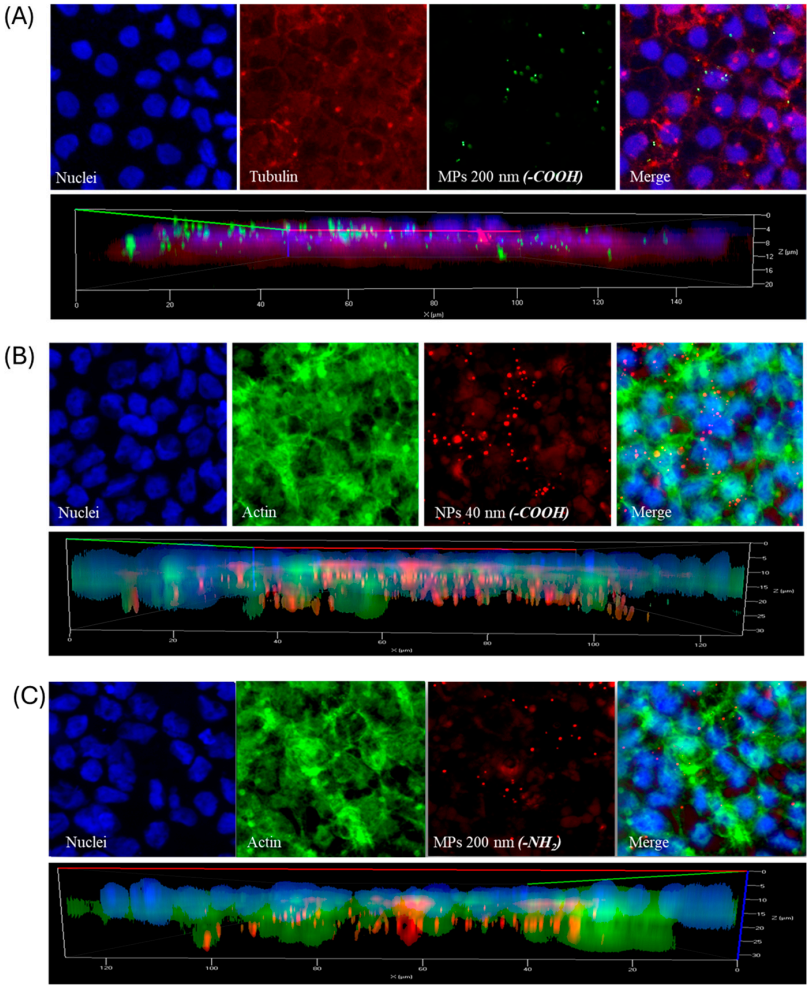

Figure 7. Confocal microscopy images acquired after staining with (**A**) anti-tubulin (red labeling acquired with the 555 laser) to label the microtubules of cytoskeleton. Polystyrene microbeads are shown in green (green labeling acquired with the 488 laser), and nuclei are stained in blue with DAPI (blue labeling acquired with the 405 laser). (**B**,**C**) FITC-conjugated phalloidin (green labeling acquired with the 488 laser) was used to label the microfilaments of the cytoskeleton. Polystyrene nanobeads and microbeads are shown in red (red labeling acquired with the 555 laser), and nuclei are stained in blue with DAPI (blue labeling acquired with the 405 laser). The lower graphs in (**A**–**C**) show 3D reconstructions derived from z-stack scans of the triple-culture model.

Studies consistently report that particle size plays a decisive role in the translocation of polystyrene particles across intestinal models. Generally, nanobeads exhibit higher rates of uptake and translocation compared to larger microbeads due to their smaller size, greater surface area, and propensity for exploiting endocytic pathways such as clathrin-mediated and fast endophilin-mediated endocytosis [61–63]. In tri-culture models composed of Caco-2, HT29-MTX, and Raji B-induced M-like cells, nanoplastics not only traverse the mucus layer more efficiently but also show higher passage rates toward the basolateral compartment relative to microplastics, which are often partially retained by the mucus and cellular junctions [57]. Surface chemistry significantly influences particle interaction with intestinal cells. Carboxylate polystyrene beads, for example, demonstrate enhanced adhesion and are more readily internalized compared to non-functionalized beads, owing to their amphiphilic nature and ability to interact with hydrophilic cells [64,65]. In tri-culture models, amine-functionalized particles (positively charged) display stronger binding to negatively charged cell membranes and mucins, often resulting in different uptake patterns compared to carboxylate (negatively charged) or pristine beads. These findings have important implications for understanding human exposure to micro- and nanoplastics. The efficient internalization, especially of nanosized and surface-modified particles, raises concerns due to their potential for systemic distribution and interference with gut barrier integrity, host–microbiota interactions, and immune modulation [66]. Larger microplastics may be more likely to elicit local effects, whereas nanoplastics can reach deeper tissue layers and even enter the circulatory system, possibly impacting distant organs [67].

Overall, our results corroborate recent studies showing that optimal cellular internalization is not dictated by size alone, but by a combination of size and surface chemistry. Positively charged (-NH_2) surfaces can compensate for limitations imposed by a larger particle size, significantly boosting uptake rates. Conversely, negatively charged (-COOH) particles suffer reduced internalization regardless of particle size [68].

From a size perspective, the literature shows that smaller nanoparticles are usually taken up by cells more efficiently, as their dimensions favor endocytosis and membrane wrapping processes [51]. However, in this dataset, the 200 nm-sized NH_2-modified particles outperform even the 40 nm-sized COOH-functionalized particles in terms of uptake. This result suggests that surface chemistry, particularly the presence of NH_2 groups, can override the effect of size alone. The NH_2 groups on the particle surface impart a net positive charge, which strongly interacts with the negatively charged cell membranes, facilitating particle adhesion and uptake via endocytic pathways [52]. For the COOH-functionalized beads, the negative surface charge leads to weaker interactions with cell membranes, reducing internalization efficiency even for smaller particle sizes such as 40 nm. The 200 nm -COOH beads are internalized least efficiently, supporting the concept that both a large size and negative charge restrict cellular uptake [52].

The concept that the optimal nanoparticle size for cellular uptake may vary depending on cell type and nanoparticle material is well supported in recent research. Different cell types exhibit distinct endocytic capacities, receptor expressions, membrane compositions, and cytoskeletal arrangements, all of which modulate how efficiently they internalize nanoparticles of various sizes. For instance, cancer cells often exhibit enhanced endocytic activity compared to normal cells, which can shift the size range at which uptake is maximized. Moreover, the physicochemical properties of the nanoparticle material, such as core composition, surface coating, density, and rigidity, impact how cells interact with and internalize these particles. For example, heavier or denser nanoparticles may be internalized differently than lighter ones of the same size, and surface coatings may alter protein corona formation, thereby influencing recognition by cell surface receptors.

3.6. Role of Protein Corona

When particles enter a biological fluid or the environment, biomolecules like proteins, lipids, ions, and other small molecules bind to the surface, changing the chemical properties and further modulating particle uptake and toxicity. In fact, the corona layer completely changes the particles' interactions with cells and, in turn, the cells' responses. Among molecules forming layers around particles, proteins are more abundant; so, we decided to compare the protein profiles of our barrier model and the Caco-2 cell mono-culture.

It should be noted that the protein corona characterization performed in this study is qualitative in nature and was not intended to provide a quantitative or normalized assessment of protein abundance. The observed differences in protein corona composition should therefore be interpreted as descriptive and indicative of distinct biological identities acquired by particles under different experimental conditions, rather than as direct mechanistic determinants of penetration or barrier disruption.

The analysis of the protein corona profiles revealed clear differences related to both particle size and surface chemistry, as well as to the culture model used for incubation (Figure 8). The 40 nm -COOH beads (Lane 2), when exposed to the barrier model based on the tri-culture composed of Caco-2, HT29, and Raji B cells, displayed a markedly higher abundance of high-molecular-weight proteins, including putative adhesion proteins, large glycoproteins, and protein complexes. This effect may be attributed to particles' higher curvature and surface-to-volume ratio, which facilitate the assembly of large protein complexes, and to a specific affinity of the negatively charged –COOH groups for large proteins present in the complex biological environment of the tri-culture. These findings align with Lundqvist et al. (2008) [38], who demonstrated that smaller particles exhibit increased and more selective binding of multidomain proteins compared to larger particles, primarily due to enhanced surface curvature. Further, Wang et al. (2020) [69] and Rampado et al. (2022) [70] corroborate that surface chemistry crucially determines corona composition; negatively charged surfaces preferentially adsorb large, glycosylated, or hydrophobic proteins, consistent with the selective enrichment observed here for the -COOH-functionalized nanobeads.

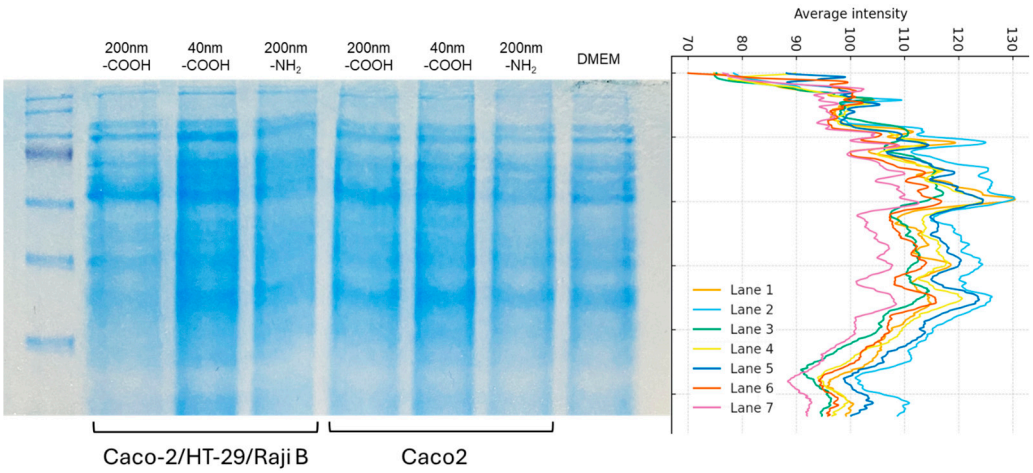

Figure 8. SDS-PAGE showing the protein corona of MNBs after 24 h of incubation with tri-culture or Caco-2 alone. The standard ladder is given on the left side; from the top to the bottom: 180 KDa, 140 KDa, 100 KDa, 75 KDa, 60 KDa, 45 KDa, and 35 KDa. The sample order is indicated above the lanes. DMEM: culture medium control. On the right: profile of average band intensities indicating the difference in the amount of protein corona on the MNB surface and identified with different colors as reported in the legend. Lane 1: 200 nm -COOH; Lane 2: 40 nm -COOH; Lane 3: 200 nm -NH_2 (from MNBs in incubation with 3D model); Lane 4: 200 nm -COOH; Lane 5: 40 nm -COOH; Lane 6: 200 nm -NH_2 (from MNBs in incubation with Caco-2 alone); Lane 7: DMEM.

In contrast, the 200 nm -NH_2 beads (Lane 3) preferentially bind to smaller proteins. The amine surface, positively charged under physiological conditions, may favor electrostatic interactions with negatively charged, low-molecular-weight proteins or soluble fragments released by the cells within the tri-culture. This matches observations by Abstiens et al. (2019) [71], who reported that amine-modified surfaces show affinity for low-molecular-weight hydrophilic proteins. The 200 nm COOH beads (Lane 1) exhibited a more heterogeneous corona, consisting of a combination of small- and medium-sized proteins, with a relatively lower accumulation of high-molecular-weight species compared with the 40 nm -COOH sample. This phenomenon can be explained by the lower curvature and reduced surface-to-volume ratio of larger particles. Larger particles provide a flatter surface that tends to favor the adsorption of proteins with diverse sizes but may be less conductive to stabilizing large, multidomain proteins or complexes. Monopoli et al. (2012) [72] demonstrated that nanoparticle size influences protein binding kinetics and affinity hierarchies, producing coronas with distinct profiles depending on particle dimensions. According to Gonzalez Solveyra et al. (2022) [73], the interplay between surface curvature and protein conformation affects adsorption stability—flatter surfaces of larger particles tend to favor loosely bound, smaller proteins that might be displaced over time, whereas a high curvature promotes the stable binding of large, folded, and glycosylated proteins.

From a biological perspective, the strong enrichment of high-molecular-weight proteins on the 40 nm -COOH beads in the tri-culture suggests that a complex cellular environment containing enterocytes, mucus-secreting cells, and immune-like cells promotes the secretion or retention of large proteins and complexes that preferentially associate with small, negatively charged nanoparticles. Such differences in corona composition may influence nanoparticle recognition and immunoreactivity in biological systems. Studies using multi-cellular intestinal models have demonstrated that mucins, secreted by goblet cells like HT29, readily adsorb onto nanoparticle surfaces to form a protein corona that significantly alters their biological fate and cellular interactions. Yang et al. (2024) [74] specifically showed that mucin-derived protein coronas act as both "spear and shield," modulating nanoparticle transcellular transport in enterocytes and enhancing intracellular trafficking through altered protein composition. The presence of immune-like cells further enriches the extracellular environment with immune-related proteins, including complement components, immunoglobulins, and acute-phase proteins, which preferentially bind to nanoparticles and fundamentally alter their biological identity [75].

In the Caco-2 mono-culture, the 200 nm -COOH beads (Lane 4) showed a pronounced enrichment of high-molecular-weight proteins, similar to that observed in the 40 nm -COOH beads under tri-culture conditions. This indicates that even the epithelial cell line alone produces large proteins capable of interacting with carboxylated surfaces. The 40 nm -COOH beads in mono-culture (Lane 5), however, appeared less enriched in large proteins than their tri-culture counterpart, implying that the presence of HT29 and Raji B cells provides additional secreted factors that promote the adsorption of large proteins onto small nanobeads. The 200 nm -NH_2 beads in mono-culture (Lane 6) exhibited the weakest signal, suggesting a less abundant or less diverse protein corona in the absence of the additional cell types present in the tri-culture. This finding is well supported by the literature on epithelial cell secretion and culture media composition. Caco-2 cells, when differentiated into mature enterocytes, secrete several large proteins and extracellular matrix (ECM) components that readily interact with nanoparticle surfaces. DiMarco et al. (2017) [76] showed that Caco-2 cells produce and deposit fibronectin and other ECM proteins that form a complex microenvironment capable of engaging large, glycosylated proteins with nanoparticles. Moreover, Caco-2 cells express and secrete various adhesion molecules, including E-cadherin, occludin, and claudins, as well as large glycoproteins involved in

cell–cell interactions, all of which are substantial macromolecules that can readily adsorb to carboxylated surfaces and have high affinity for -COOH functionalized nanobeads.

When directly comparing tri-culture and mono-culture conditions for each particle type, further trends emerged. The 200 nm -COOH beads (Lanes 1 and 4) displayed distinct profiles: in mono-culture, the corona was dominated by high-molecular-weight proteins, whereas in tri-culture the profile was more balanced and included additional mid- and low-molecular-weight components. This suggests that proteins secreted by HT29 and Raji B cells, such as mucins or small peptides, may compete with larger proteins for adsorption sites. For the 40 nm -COOH beads (Lanes 2 and 5), the tri-culture induced a substantial enrichment in high-molecular-weight proteins, indicating that additional extracellular factors or immune-derived proteins promote the association of large protein complexes with smaller nanoparticles.

Baimanov et al. (2022) [77] demonstrated that protein corona formation is a dynamic process rather than an immediate one. Initially, small nanoparticles bind mainly to highly abundant proteins, but over time these are replaced by proteins with higher affinity for the nanoparticle surface. In the tri-culture system, mucin-rich secretions and immune-derived protein complexes provide a rich source of large, biologically active macromolecules that can strongly associate with small, negatively charged nanoparticles. Finally, the 200 nm -NH_2 beads (Lanes 3 and 6) exhibited more intense low-molecular-weight bands in tri-culture than in mono-culture, implying that the presence of multiple cell types enriches the medium with negatively charged small proteins or peptides that preferentially adsorb to amine-functionalized surfaces. Yu et al. (2020) [78] showed that the nature of protein adsorption and exchange is intimately tied to both surface properties and the protein pool available; hydrophilic charged surfaces display higher protein exchange rates and greater sensitivity to environmental protein composition. Indeed, the protein corona exhibits a "memory effect," whereby particles transitioning from one biological context to another retain elements of their original corona while gradually acquiring new species, a phenomenon that becomes more pronounced when the environmental protein pool changes dramatically.

4. Conclusions

This study successfully developed and optimized a physiologically relevant 3D in vitro intestinal barrier model integrating enterocytes, mucus-secreting goblet cells, and M-cell-like immune components. Compared to mono-culture and co-culture systems, the tri-culture model exhibited enhanced barrier functionality and structural complexity, as confirmed by TEER measurements and the expression of key marker proteins. The use of this advanced model enabled a more realistic evaluation of size- and surface chemistry-dependent interactions between polystyrene micro- and nanoplastics and the intestinal epithelium.

Within this context, our findings demonstrate that both particle size and surface functionalization play a central role in shaping nanoparticle behavior at the gut interface. Smaller nanoparticles, particularly those with a diameter of 40 nm, provided higher surface curvature and relative surface area, favoring the stabilization and recruitment of large multidomain proteins and protein complexes when available. Notably, 40 nm -COOH-functionalized nanobeads in the tri-culture system were enriched in high-molecular-weight proteins, supporting the notion that small, negatively charged particles efficiently attract large protein assemblies from complex biological environments. Surface chemistry further modulated corona composition: negatively charged carboxyl groups promoted interactions with positively charged protein domains, enhancing the adsorption of large, hydrophobic, or glycosylated proteins, whereas positively charged amine groups preferentially associated

with smaller, negatively charged, or more hydrophilic proteins, resulting in less abundant or more selective protein coronas.

Importantly, the influence of the cellular microenvironment emerged as a key determinant of nanoparticle biological identity. The tri-culture system introduced mucins, extracellular matrix components, immune-related proteins, and secreted factors absent in simpler models, profoundly altering both the qualitative and quantitative composition of the protein corona. These results underscore that nanoparticle–biological interactions cannot be fully understood based solely on physicochemical properties but must also consider the complexity of the surrounding cellular environment.

Overall, this work advances our understanding of how micro- and nanoplastics interact with the intestinal barrier and highlights the necessity of employing complex in vitro systems to capture the multifaceted nature of nanoparticle–biological interfaces. The tri-culture model presented here offers a robust and physiologically relevant platform for future mechanistic studies investigating microplastic bioavailability, toxicity, and transport. In particular, future work will address a full dose–response curve and multiple exposure durations, including repeated and chronic exposures, to better capture the long-term and low-dose effects of micro and nanoplastics on intestinal barrier function and host responses.

Author Contributions: Conceptualization, S.M. and E.P.; methodology, S.M. and E.C.; validation, S.M., E.P., and E.C.; formal analysis, S.M. and E.C.; investigation, S.M. and E.C.; data curation, S.M. and E.P.; writing—original draft preparation, S.M.; writing—review and editing, S.M. and E.P.; visualization, E.P.; supervision, E.P. All authors have read and agreed to the published version of the manuscript.

Funding: This research was funded by Italian Ministry of Education, University and Research MIUR, PON 2014–2020, grant number AIM 1848751-2; Linea 1.

Institutional Review Board Statement: Not applicable.

Informed Consent Statement: Not applicable.

Data Availability Statement: The data presented in this study are available on request from the corresponding authors.

Conflicts of Interest: The authors declare no conflicts of interest.

Abbreviations

The following abbreviations are used in this manuscript:

BSA	Bovine Serum Albumin
Caco-2	Human Colorectal Adenocarcinoma Cell Line
CO_2	Carbon Dioxide
-COOH	Carboxylate (Functional Group)
DLS	Dynamic Light Scattering
DMEM	Dulbecco's Modified Eagle Medium
DAPI	4′,6-Diamidino-2-Phenylindole
FBS	Fetal Bovine Serum
FITC	Fluorescein Isothiocyanate
HT29-MTX	HT29 Mucus-Secreting Cell
IU	International Unit
M	Mucus
MNBs	Micro- And Nanobeads
MPs	Microplastics
MTT	3-(4,5-Dimethylthiazol-2-Yl)-2,5-Diphenyltetrazolium Bromide
$-NH_2$	Amine (Functional Group)
NPs	Nanoplastics

PAHs	Polycyclic Aromatic Hydrocarbons
PBS	Phosphate-Buffered Saline
PS	Polystyrene
Raji B	Raji B Cell Line
RGR	Relative Growth Rate
RPMI	Roswell Park Memorial Institute Medium
RT	Room Temperature
SDS-PAGE	Sodium Dodecyl Sulfate-Polyacrylamide Gel Electrophoresis
SEM	Scanning Electron Microscopy
SD	Standard Deviation
TEER	Transepithelial Electrical Resistance
TEM	Transmission Electron Microscopy
WGA	Wheat Germ Agglutinin
ZO-1	Zonula Occludens-1

References

1. Ziani, K.; Ioniță-Mîndrican, C.-B.; Mititelu, M.; Neacșu, S.M.; Negrei, C.; Moroșan, E.; Drăgănescu, D.; Preda, O.-T. Microplastics: A Real Global Threat for Environment and Food Safety: A State of the Art Review. *Nutrients* **2023**, *15*, 617. [CrossRef] [PubMed]
2. Smith, M.; Love, D.C.; Rochman, C.M.; Neff, R.A. Microplastics in Seafood and the Implications for Human Health. *Curr. Environ. Health Rep.* **2018**, *5*, 375–386. [CrossRef] [PubMed]
3. Osman, A.I.; Hosny, M.; Eltaweil, A.S.; Omar, S.; Elgarahy, A.M.; Farghali, M.; Yap, P.-S.; Wu, Y.-S.; Nagandran, S.; Batumalaie, K.; et al. Microplastic Sources, Formation, Toxicity and Remediation: A Review. *Environ. Chem. Lett.* **2023**, *21*, 2129–2169. [CrossRef] [PubMed]
4. Galloway, T.S.; Cole, M.; Lewis, C. Interactions of Microplastic Debris Throughout the Marine Ecosystem. *Nat. Ecol. Evol.* **2017**, *1*, 0116. [CrossRef]
5. Bergmann, M.; Mützel, S.; Primpke, S.; Tekman, M.B.; Trachsel, J.; Gerdts, G. White and Wonderful? Microplastics Prevail in Snow from the Alps to the Arctic. *Sci. Adv.* **2019**, *5*, eaax1157. [CrossRef]
6. Koelmans, A.A.; Nor, N.H.M.; Hermsen, E.; Kooi, M.; Mintenig, S.M.; De France, J. Microplastics in Freshwaters and Drinking Water: Critical Review and Assessment of Data Quality. *Water Res.* **2019**, *155*, 410–422. [CrossRef]
7. Wright, S.L.; Thompson, R.C.; Galloway, T.S. The Physical Impacts of Microplastics on Marine Organisms: A Review. *Environ. Pollut.* **2013**, *178*, 483–492. [CrossRef]
8. Zhang, T.; Wang, Z.; Wu, Y.; Zhu, S.; Su, J. Interactions of Micro-and Nanoplastics with Biomolecules: From Public Health to Protein Corona Effect and Beyond. *J. Phys. Chem. B* **2025**, *129*, 5355–5374. [CrossRef]
9. Viana, M.; Tonin, F.S.; Ladeira, C. Assessing the Impact of Nanoplastics in Biological Systems: Systematic Review of In Vitro Animal Studies. *J. Xenobiot.* **2025**, *15*, 75. [CrossRef]
10. Hartmann, N.B.; Huffer, T.; Thompson, R.C.; Hassellov, M.; Verschoor, A.; Daugaard, A.E.; Rist, S.; Karlsson, T.; Brennholt, N.; Cole, M. Are We Speaking the Same Language? Recommendations for a Definition and Categorization Framework for Plastic Debris. *Environ. Sci. Technol.* **2019**, *53*, 1039–1047. [CrossRef]
11. Furfaro, G.; D'Elia, M.; Mariano, S.; Trainito, E.; Solca, M.; Piraino, S.; Belmonte, G. SEM/EDX Analysis of Stomach Contents of a Sea Slug Snacking on a Polluted Seafloor Reveal Microplastics as a Component of Its Diet. *Sci. Rep.* **2022**, *12*, 10244. [CrossRef] [PubMed]
12. Arias, A.H.; Girones, L.; Oliva, A.L.; Marcovecchio, J.E.; Valdivia, A.L.; Malafaia, G. Organic Pollutants and Plastics Threatening the Ocean's Health an Urgent Issue. In *Volume 2: Marine Ecology*; CRC Press: Boca Raton, FL, USA, 2025; pp. 94–103.
13. Müller, K.; Unice, K.; Panko, J.; Ferrari, B.J.; Breider, F.; Wagner, S. Risk Assessment of Tire Wear in the Environment—A Literature Review. *Environ. Sci. Process. Impacts* **2025**, *27*, 2212–2232. [CrossRef]
14. Zhao, J.; Lan, R.; Tan, H.; Wang, J.; Ma, Y.; Chen, Q.; Jiang, F.; Wang, Z.; Xing, B. Detection and Characterization of Microplastics and Nanoplastics in Biological Samples. *Nat. Rev. Bioeng.* **2025**, *3*, 1019–1033. [CrossRef]
15. Li, G.; Lv, M.; Yu, H.; Zhang, H.; Zhang, D.; Li, Q.; Wang, L.; Wu, Y. Integration of physiology, microbiota and metabolomics reveals toxic response of zebrafish gut to co-exposure to polystyrene nanoplastics and arsenic. *Aquat. Toxicol.* **2025**, *278*, 107172. [CrossRef]
16. Liu, L.; Xu, K.; Zhang, B.; Ye, Y.; Zhang, Q.; Jiang, W. Cellular Internalization and Release of Polystyrene Microplastics and Nanoplastics. *Sci. Total Environ.* **2021**, *779*, 146523. [CrossRef]

17. Xie, Y.; Lyu, Y.; Irshad, S.; Liu, X.; Jiang, Y.; Sun, Y.; Zhang, Z.; Wei, H.; He, H.; An, C. Combined Interactions and Ecotoxicological Effects of Micro/Nanoplastics and Organic Pollutants in Soil–Plant Systems: A Critical Overview. *Environ. Sci. Adv.* **2025**, *4*, 1166–1180. [CrossRef]
18. Hou, G.; Zhao, X.; Zhao, T.; Wu, X.; Pu, S.; Tang, Z.; Wu, F. The Adsorption of PAHs on Microplastics and Desorption in the Simulated Human Digestive System. *Chem. Eng. J.* **2023**, *473*, 145157. [CrossRef]
19. Accinelli, C.; Abbas, H.K.; Shier, W.T.; Vicari, A.; Little, N.S.; Aloise, M.R.; Giacomini, S. Degradation of Microplastic Seed Film-Coating Fragments in Soil. *Chemosphere* **2019**, *226*, 645–650. [CrossRef]
20. He, S.; Tong, J.; Xiong, W.; Xiang, Y.; Peng, H.; Wang, W.; Yang, Y.; Ye, Y.; Hu, M.; Yang, Z. Microplastics Influence the Fate of Antibiotics in Freshwater Environments: Biofilm Formation and Its Effect on Adsorption Behavior. *J. Hazard. Mater.* **2023**, *442*, 130078. [CrossRef]
21. Debroy, A.; George, N.; Mukherjee, G. Role of Biofilms in the Degradation of Microplastics in Aquatic Environments. *J. Chem. Technol. Biotechnol.* **2022**, *97*, 3271–3282. [CrossRef]
22. Ahn, H.M.; Park, J.O.; Lee, H.-J.; Lee, C.; Chun, H.; Kim, K.B. SERS Detection of Surface-Adsorbent Toxic Substances of Microplastics Based on Gold Nanoparticles and Surface Acoustic Waves. *RSC Adv.* **2024**, *14*, 2061–2069. [CrossRef] [PubMed]
23. Xie, H.; Wang, X.; Cui, L.; Chen, R.; Zhao, R.; Yu, Y.; Chen, D.; Yu, Y.-L.; Li, B.; Li, Y.-F. Life-Long Impacts of Nanoplastics to Rice Plant (*Oryza sativa* L.): Decreased Grain Yield with Perturbed Metallome and Soil Microbiome. *J. Hazard. Mater.* **2025**, *494*, 138787. [CrossRef] [PubMed]
24. Ryan, P.G. Ingestion of Plastics by Marine Organisms. In *Hazardous Chemicals Associated with Plastics in the Marine Environment*; Springer: Berlin/Heidelberg, Germany, 2016; pp. 235–266.
25. Zhao, X.; Sun, J.; Zhou, L.; Teng, M.; Zhao, L.; Li, Y.; Wu, F. Defining the Size Ranges of Polystyrene Nanoplastics According to Their Ability to Cross Biological Barriers. *Environ. Sci. Nano* **2023**, *10*, 2634–2645. [CrossRef]
26. Kim, K.; Yoon, H.; Choi, J.S.; Jung, Y.-J.; Park, J.-W. Chronic Effects of Nano and Microplastics on Reproduction and Development of Marine Copepod Tigriopus japonicus. *Ecotoxicol. Environ. Saf.* **2022**, *243*, 113962. [CrossRef]
27. Sun, A.; Wang, W.-X. Human Exposure to Microplastics and Its Associated Health Risks. *Environ. Health* **2023**, *1*, 139–149. [CrossRef] [PubMed]
28. Tang, K.H.D.; Li, R.; Li, Z.; Wang, D. Health Risk of Human Exposure to Microplastics: A Review. *Environ. Chem. Lett.* **2024**, *22*, 1155–1183. [CrossRef]
29. Hua, X.; Wang, D. Cellular Uptake, Transport, and Organelle Response after Exposure to Microplastics and Nanoplastics: Current Knowledge and Perspectives for Environmental and Health Risks. *Rev. Environ. Contam. Toxicol.* **2022**, *260*, 12. [CrossRef]
30. Khan, A.; Jia, Z. Recent Insights into Uptake, Toxicity, and Molecular Targets of Microplastics and Nanoplastics Relevant to Human Health Impacts. *Iscience* **2023**, *26*, 106061. [CrossRef]
31. Mariano, S.; Tacconi, S.; Fidaleo, M.; Rossi, M.; Dini, L. Micro and Nanoplastics Identification: Classic Methods and Innovative Detection Techniques. *Front. Toxicol.* **2021**, *3*, 636640. [CrossRef]
32. Ivleva, N.P. Chemical Analysis of Microplastics and Nanoplastics: Challenges, Advanced Methods, and Perspectives. *Chem. Rev.* **2021**, *121*, 11886–11936. [CrossRef]
33. Rivera-Rivera, D.M.; Quintanilla-Villanueva, G.E.; Luna-Moreno, D.; Sánchez-Álvarez, A.; Rodríguez-Delgado, J.M.; Cedillo-González, E.I.; Kaushik, G.; Villarreal-Chiu, J.F.; Rodríguez-Delgado, M.M. Exploring Innovative Approaches for the Analysis of Micro-and Nanoplastics: Breakthroughs in (Bio) Sensing Techniques. *Biosensors* **2025**, *15*, 44. [CrossRef]
34. Onyena, A.P.; Aniche, D.C.; Ogbolu, B.O.; Rakib, M.R.J.; Uddin, J.; Walker, T.R. Governance Strategies for Mitigating Microplastic Pollution in the Marine Environment: A Review. *Microplastics* **2021**, *1*, 15–46. [CrossRef]
35. Al-Azzawi, M.S.; Kefer, S.; Weißer, J.; Reichel, J.; Schwaller, C.; Glas, K.; Knoop, O.; Drewes, J.E. Validation of Sample Preparation Methods for Microplastic Analysis in Wastewater Matrices—Reproducibility and Standardization. *Water* **2020**, *12*, 2445. [CrossRef]
36. Gambardella, C.; Morgana, S.; Bramini, M.; Rotini, A.; Manfra, L.; Migliore, L.; Piazza, V.; Garaventa, F.; Faimali, M. Ecotoxicological Effects of Polystyrene Microbeads in a Battery of Marine Organisms Belonging to Different Trophic Levels. *Mar. Environ. Res.* **2018**, *141*, 313–321. [CrossRef]
37. Schimpel, C.; Teubl, B.; Absenger, M.; Meindl, C.; Fröhlich, E.; Leitinger, G.; Zimmer, A.; Roblegg, E. Development of an Advanced Intestinal In Vitro Triple Culture Permeability Model to Study Transport of Nanoparticles. *Mol. Pharm.* **2014**, *11*, 808–818. [CrossRef]
38. Lundqvist, M.; Stigler, J.; Elia, G.; Lynch, I.; Cedervall, T.; Dawson, K.A. Nanoparticle Size and Surface Properties Determine the Protein Corona with Possible Implications for Biological Impacts. *Proc. Natl. Acad. Sci. USA* **2008**, *105*, 14265–14270. [CrossRef] [PubMed]
39. Lozoya-Agullo, I.; Araujo, F.; Gonzalez-Alvarez, I.; Merino-Sanjuan, M.; Gonzalez-Alvarez, M.; Bermejo, M.; Sarmento, B. Usefulness of Caco-2/HT29-MTX and Caco-2/HT29-MTX/Raji B Coculture Models to Predict Intestinal and Colonic Permeability Compared to Caco-2 Monoculture. *Mol. Pharm.* **2017**, *14*, 1264–1270. [CrossRef] [PubMed]

40. Adesina, P.A.; Ooka, M.; TeKrony, C.; Xia, M. Emerging Advances in Intestinal Models for In Vitro Preclinical Research. *Am. J. Physiol.-Gastrointest. Liver Physiol.* **2025**, *329*, G403–G416. [CrossRef] [PubMed]
41. Moyer, H.L.; Vergara, L.; Stephan, C.; Sakolish, C.; Lin, H.-C.; Chiu, W.A.; Villenave, R.; Hewitt, P.; Ferguson, S.S.; Rusyn, I. Human Small Intestinal Tissue Models to Assess Barrier Permeability: Comparative Analysis of Caco-2 Cells, Jejunal and Duodenal Enteroid-Derived Cells, and EpiIntestinalTM Tissues in Membrane-Based Cultures with and Without Flow. *Bioengineering* **2025**, *12*, 809. [CrossRef]
42. Donetti, E.; Bendinelli, P.; Correnti, M.; Gammella, E.; Recalcati, S.; Ferraretto, A. Caco2/HT29 In Vitro Cell Co-Culture: Barrier Integrity, Permeability, and Tight Junctions' Composition During Progressive Passages of Parental Cells. *Biology* **2025**, *14*, 267. [CrossRef]
43. Fioroni, N.; de León, M.D.C.P.; Leconte, N.; Mouquet-Rivier, C.; Guzman, C.; Boudard, F.; Dhuique-Mayer, C.; Collin, M.; Deglos, A.; Reboul, E. Development of an In Vitro Triculture Model of Intestine Inflammation to Assess the Immunomodulatory Properties of Cassava and Roselle, Two African Green Leafy Vegetables. *NFS J.* **2025**, *38*, 100213. [CrossRef]
44. Supjaroen, P.; Niamsi, W.; Thummarati, P.; Laiwattanapaisal, W. An In Vitro Cell Model of Intestinal Barrier Function Using a Low-Cost 3D-Printed Transwell Device and Paper-Based Cell Membrane. *Int. J. Mol. Sci.* **2025**, *26*, 2524. [CrossRef] [PubMed]
45. Rejinold, S.; Kim, J.-Y.; Jin, G.; Choi, G.; Choy, J.-H. Transport Mechanisms of 2D Nanoparticles across a Human Follicle-Associated Epithelium Model. *ACS Omega* **2025**, *10*, 40901. [CrossRef]
46. Wang, Z.-H.; Zeng, X.; Huang, W.; Yang, Y.; Zhang, S.; Yang, M.; Liu, H.; Zhao, F.; Li, A.; Zhang, Z. Bioactive Nanomotor Enabling Efficient Intestinal Barrier Penetration for Colorectal Cancer Therapy. *Nat. Commun.* **2025**, *16*, 1678. [CrossRef]
47. Marescotti, D.; Lo Sasso, G.; Guerrera, D.; Renggli, K.; Ruiz Castro, P.A.; Piault, R.; Jaquet, V.; Moine, F.; Luettich, K.; Frentzel, S. Development of an Advanced Multicellular Intestinal Model for Assessing Immunomodulatory Properties of Anti-Inflammatory Compounds. *Front. Pharmacol.* **2021**, *12*, 639716. [CrossRef] [PubMed]
48. Santoni, M.; Piccinini, G.; Liguori, G.; Randi, M.R.; Baroncini, M.; Milani, L.; Danesi, F. Enhanced Intestinal Epithelial Co-Culture Model with Orbital Mechanical Stimulation: A Proof-of-Concept Application in Food Nanotoxicology. *Front. Mol. Biosci.* **2025**, *11*, 1529027. [CrossRef]
49. Vincentini, O.; Prota, V.; Cecchetti, S.; Bertuccini, L.; Tinari, A.; Iosi, F.; De Angelis, I. Towards the Standardization of Intestinal in Vitro Advanced Barrier Model for Nanoparticles Uptake and Crossing: The SiO_2 Case Study. *Cells* **2022**, *11*, 3357. [CrossRef]
50. Masuda, K.; Kajikawa, A.; Igimi, S. Establishment and Evaluation of an in Vitro M Cell Model Using C2BBe1 Cells and Raji Cells. *Biosci. Microflora* **2011**, *30*, 37–44. [CrossRef]
51. Chithrani, B.D.; Ghazani, A.A.; Chan, W.C. Determining the Size and Shape Dependence of Gold Nanoparticle Uptake into Mammalian Cells. *Nano Lett.* **2006**, *6*, 662–668. [CrossRef]
52. Sanità, G.; Carrese, B.; Lamberti, A. Nanoparticle Surface Functionalization: How to Improve Biocompatibility and Cellular Internalization. *Front. Mol. Biosci.* **2020**, *7*, 587012. [CrossRef]
53. Bannunah, A.M.; Vllasaliu, D.; Lord, J.; Stolnik, S. Mechanisms of Nanoparticle Internalization and Transport across an Intestinal Epithelial Cell Model: Effect of Size and Surface Charge. *Mol. Pharm.* **2014**, *11*, 4363–4373. [CrossRef]
54. DeLoid, G.M.; Cohen, J.M.; Pyrgiotakis, G.; Demokritou, P. Preparation, Characterization, and In Vitro Dosimetry of Dispersed, Engineered Nanomaterials. *Nat. Protoc.* **2017**, *12*, 355–371. [CrossRef] [PubMed]
55. Bouwmeester, H.; van der Zande, M.; Jepson, M.A. Effects of Food-borne Nanomaterials on Gastrointestinal Tissues and Microbiota. *Wiley Interdiscip. Rev. Nanomed. Nanobiotechnol.* **2018**, *10*, e1481. [CrossRef] [PubMed]
56. Banerjee, A.; Lee, J.; Mitragotri, S. Intestinal Mucoadhesive Devices for Oral Delivery of Insulin. *Bioeng. Transl. Med.* **2016**, *1*, 338–346. [CrossRef]
57. Marcellus, K.A.; Prescott, D.; Scur, M.; Ross, N.; Gill, S.S. Exposure of Polystyrene Nano-and Microplastics in Increasingly Complex in Vitro Intestinal Cell Models. *Nanomaterials* **2025**, *15*, 267. [CrossRef]
58. Zhang, K.-D.; Wang, Z.; Zhang, H.-J.; Fang, H.-T.; Tan, Q.-G.; Miao, A.-J. Toxicokinetic-Toxicodynamic Modeling Reveals the Ecological Risks of Differently-Sized Polystyrene Nanoplastics. *Environ. Pollut.* **2025**, *383*, 126792. [CrossRef]
59. Kustra, A.; Zając, M.; Bednarczyk, P.; Maliszewska-Olejniczak, K. Exposure to Polystyrene Nanoparticles Leads to Dysfunction in DNA Repair Mechanisms in Caco-2 Cells. *Biol. Res.* **2025**, *58*, 49. [CrossRef]
60. Domenech, J.; Marcos, R. Pathways of Human Exposure to Microplastics, and Estimation of the Total Burden. *Curr. Opin. Food Sci.* **2021**, *39*, 144–151. [CrossRef]
61. Choi, H.; Kaneko, S.; Suzuki, Y.; Inamura, K.; Nishikawa, M.; Sakai, Y. Size-Dependent Internalization of Microplastics and Nanoplastics in Human Intestinal Cells. *J. Hazard. Mater.* **2024**, *473*, 134706.
62. DeLoid, G.M.; Yang, Z.; Bazina, L.; Kharaghani, D.; Sadrieh, F.; Demokritou, P. Mechanisms of Ingested Polystyrene Micro-Nanoplastics (MNPs) Uptake and Translocation in an In Vitro Tri-Culture Small Intestinal Epithelium. *J. Hazard. Mater.* **2024**, *473*, 134706. [CrossRef] [PubMed]

63. Elfers, K.; Benz, P.; Burmester, M.; Hein, S.; Hansen, K.; Sieg, H.; Böhmert, L.; Paul, M.B.; Mazzuoli-Weber, G. Effect of Nano-and Micro-Polystyrene Particles on Small Intestinal Epithelial Functions and Enteric Neuronal Activity In Vitro. *Microplast. Nanoplast.* **2025**, *5*, 3. [CrossRef]
64. Jiang, Y.; Huo, S.; Mizuhara, T.; Das, R.; Lee, Y.-W.; Hou, S.; Moyano, D.F.; Duncan, B.; Liang, X.-J.; Rotello, V.M. The Interplay of Size and Surface Functionality on the Cellular Uptake of Sub-10 Nm Gold Nanoparticles. *ACS Nano* **2015**, *9*, 9986–9993. [CrossRef]
65. Paget, V.; Dekali, S.; Kortulewski, T.; Grall, R.; Gamez, C.; Blazy, K.; Aguerre-Chariol, O.; Chevillard, S.; Braun, A.; Rat, P. Specific Uptake and Genotoxicity Induced by Polystyrene Nanobeads with Distinct Surface Chemistry on Human Lung Epithelial Cells and Macrophages. *PLoS ONE* **2015**, *10*, e0123297. [CrossRef]
66. Hsu, W.-H.; Chen, Y.-Z.; Chiang, Y.-T.; Chang, Y.-T.; Wang, Y.-W.; Hsu, K.-T.; Hsu, Y.-Y.; Wu, P.-T.; Lee, B.-H. Polystyrene Nanoplastics Disrupt the Intestinal Microenvironment by Altering Bacteria-Host Interactions through Extracellular Vesicle-Delivered microRNAs. *Nat. Commun.* **2025**, *16*, 5026. [CrossRef] [PubMed]
67. Catalán, J.; Afanou, A.K.; Arranz, J.A.; Riaza, A.B.; Banić, I.; Dirven, H.; Estrela-Lopis, I.; Hernández, A.; Kanerva, T.; Laforsch, C. An Integrated Approach to Assess Exposure and Early Health Effects in Human Populations Exposed to Micro-and Nanoplastics. *NanoImpact* **2025**, *40*, 100600. [CrossRef]
68. Moscatiello, G.Y.; Natale, C.; Inserra, M.; Morelli, A.; Russo, L.; Battajini, N.; Sironi, L.; Panzeri, D.; Corbelli, A.; De Luigi, A. The Surface Charge Both Influences the Penetration and Safety of Polystyrene Nanoparticles despite the Protein Corona Formation. *Environ. Sci. Nano* **2025**, *12*, 2857–2870. [CrossRef]
69. Wang, L.; Hartel, N.; Ren, K.; Graham, N.A.; Malmstadt, N. Effect of Protein Corona on Nanoparticle–Plasma Membrane and Nanoparticle–Biomimetic Membrane Interactions. *Environ. Sci. Nano* **2020**, *7*, 963–971. [CrossRef]
70. Rampado, R.; Crotti, S.; Caliceti, P.; Pucciarelli, S.; Agostini, M. Recent Advances in Understanding the Protein Corona of Nanoparticles and in the Formulation of "Stealthy" Nanomaterials. *Front. Bioeng. Biotechnol.* **2020**, *8*, 166. [CrossRef]
71. Abstiens, K.; Figueroa, S.M.; Gregoritza, M.; Goepferich, A.M. Interaction of Functionalized Nanoparticles with Serum Proteins and Its Impact on Colloidal Stability and Cargo Leaching. *Soft Matter* **2019**, *15*, 709–720. [CrossRef]
72. Monopoli, M.P.; Aberg, C.; Salvati, A.; Dawson, K.A. Biomolecular coronas provide the biological identity of nanosized materials. In *Nano-Enabled Medical Applications*; Jenny Stanford Publishing: Singapore, 2020; pp. 205–229.
73. Gonzalez Solveyra, E.; Thompson, D.H.; Szleifer, I. Proteins Adsorbing onto Surface-Modified Nanoparticles: Effect of Surface Curvature, PH, and the Interplay of Polymers and Proteins Acid–Base Equilibrium. *Polymers* **2022**, *14*, 739. [CrossRef]
74. Yang, D.; Feng, Y.; Yuan, Y.; Zhang, L.; Zhou, Y.; Midgley, A.C.; Wang, Y.; Liu, N.; Li, G.; Yao, X. Protein Coronas Derived from Mucus Act as Both Spear and Shield to Regulate Transferrin Functionalized Nanoparticle Transcellular Transport in Enterocytes. *ACS Nano* **2024**, *18*, 7455–7475. [CrossRef]
75. Shan, H.; Guo, Y.; Li, J.; Liu, Z.; Chen, S.; Dashnyam, B.; McClements, D.J.; Cao, C.; Xu, X.; Yuan, B. Impact of Whey Protein Corona Formation around TiO_2 Nanoparticles on Their Physiochemical Properties and Gastrointestinal Fate. *J. Agric. Food Chem.* **2024**, *72*, 4958–4976. [CrossRef] [PubMed]
76. DiMarco, R.L.; Hunt, D.R.; Dewi, R.E.; Heilshorn, S.C. Improvement of Paracellular Transport in the Caco-2 Drug Screening Model Using Protein-Engineered Substrates. *Biomaterials* **2017**, *129*, 152–162. [CrossRef] [PubMed]
77. Baimanov, D.; Wang, J.; Zhang, J.; Liu, K.; Cong, Y.; Shi, X.; Zhang, X.; Li, Y.; Li, X.; Qiao, R. In Situ Analysis of Nanoparticle Soft Corona and Dynamic Evolution. *Nat. Commun.* **2022**, *13*, 5389. [CrossRef] [PubMed]
78. Yu, Q.; Zhao, L.; Guo, C.; Yan, B.; Su, G. Regulating Protein Corona Formation and Dynamic Protein Exchange by Controlling Nanoparticle Hydrophobicity. *Front. Bioeng. Biotechnol.* **2020**, *8*, 210. [CrossRef]